

# Pulsar Timing

Chris Williams  
Student 1607421  
HET 614

19th November 2004

## Introduction

Pulsars are neutron stars, with massive magnetic fields and prodigious spin rates, that emit pulses of energy with extreme regularity. They were discovered in radio wavelengths by Jocelyn Bell in 1967. The physics of pulsars is complex, however, from accurate measurement of the pulse period and its rate of change some estimates may be made of the underlying neutron star's age, magnetic field, and energy loss rate.

While many pulsars are visible at radio or optical wavelengths, some are dominated by X-ray emission. The study of astrophysical events in X-ray band requires high altitude or space-borne instruments because of the atmosphere's opaque nature at these wavelengths. Consequently, it was not until the space age that the discovery and study of pulsars in X-ray wavelengths became possible. Among the notable X-ray capable spacecraft is the Rossi X-ray Timing Explorer (RXTE).

This project takes data from RXTE for two pulsars detected at X-ray wavelengths and attempts to determine the key characteristics of the objects.

## Rossi X-Ray Timing Explorer

The Rossi X-ray Timing Explorer (RXTE) is a satellite observing mission launched in December 1995 and run by the NASA Goddard Space Flight Centre. The satellite was named after a leading Italian physicist in the field of X-rays, Bruno Rossi (1905–1993). As the name implies, the RXTE is primarily a platform for accurate time measurement of astronomical X-ray events.

The RXTE follows on from the earlier Einstein Observatory (AKA HEAO-2, 1978–1981) and Röntgen Satellite (ROSAT, 1991–1999) that had a more imaging focus (and problems in timing). The Chandra X-ray Observatory (1999–) has an imaging and spectroscopy focus that complements the timing functions of the RXTE.

RXTE carries three science payloads:

- Proportional Counter Array (PCA). The PCA instrument is designed for the accurate measurement of X-ray time-of-arrival in the  $1^\circ$  (full width half magnitude) field of view provided by the X-ray focusing system. The total collecting area for the instrument is  $6500 \text{ cm}^2$ . Each of five clustered counters in the PCA is sensitive to X-rays of energies 2–60 keV ( $\lambda = hc/E_{\text{ph}} = 621 \rightarrow 21 \text{ pm}$ ) and provides timing accurate to  $4.4 \mu\text{s}$  ( $2.5 \mu\text{s}$  after 29 April 1997) [2].
- High Energy X-ray Timing Experiment (HEXTE). The HEXTE instrument complements the PCA by covering X-rays from 15–250 keV ( $\lambda = 83 \rightarrow 5 \text{ pm}$ ). The sensor consists of two clusters of four scintillation detectors with sodium iodide and caesium iodide as the detector medium and  $800 \text{ cm}^2$  collecting area per cluster. Timing accuracy for HEXTE is approximately 8 microseconds.
- All-Sky Monitor (ASM). The ASM consists of three wide-angle cameras sensitive in the range 2–10 keV ( $\lambda = 621 \rightarrow 124 \text{ pm}$ ). Each camera contains a position-sensitive xenon-based proportional counter. The instrument is designed to provide 80% sky coverage every 90 minutes (one orbit).

The PCA instrument deserves a more detailed inspection since it is data from this instrument used in this project. The RXTE carries five identical proportional counters exposed along one side of the spacecraft. Incident X-rays enter the detector through an aluminised mylar window, which provides the effective 2 keV lower limit. X-rays will pass through two gas filled chambers and up to five sets of detector wires in the device. The first chamber contains propane and a set of detector wires. The next three interleaved pairs of detector anodes are immersed in a xenon atmosphere. A fourth set of wires are placed at the bottom of the xenon chamber. The top- and bottom-most detection grids are used to help eliminate spurious signals caused by the passage of charged particles through the device. X-rays will not generally travel past the first or second xenon detector grid, whereas charged particles will leave a collision induced ion trail as they pass through the entire instrument. Consequently, any correlated detection by both the outer grids can be used to flag unwanted particle events. The outer layers are called veto detectors. Below the gas chambers is a calibration X-ray source containing Americium-241.

## Science Highlights

The RXTE has been the data source underlying a large number of refereed publications, PhD theses, conference presentations, and astronomical notices. Areas of study in which the RXTE has been used include black hole

timing and spectral determination, jet phenomena, active galactic nuclei, X-ray bursts, cataclysmic variables, and, of most importance to this project, X-ray pulsars from milliseconds to seconds.

RXTE has allowed the detection and timing of numerous X-ray pulsar sources. The All-sky monitor provides 80% coverage of the sky in X-ray energies from 2–10 keV on each 90 minute Earth orbit. This allows for the rapid identification of new X-ray sources, such as outbursts from accreting material in black hole systems, to allow more detailed study. Many sources have been discovered by RXTE, and they are typically designated with XTE in the International Astronomical Union Circulars announcing each discovery.

One important, pulsar related area the RXTE has been employed in is the detection and measurement of quasi-periodic oscillation (QPO) in the X-ray emissions from a variety of sources. QPOs can betray the presence of a pulsar that is not beaming directly toward Earth. A QPO in the output from the low-mass X-ray binary system 4U 1728-34 consistent with the presence of a millisecond pulsar ( $f = 800\text{Hz}$ ) was identified by Strohmayer *et al.* in 1996 [6]. A similar detection for 4U 1636-536 was made in 1997 by Zhang *et al.* [9]. Study of QPOs in X-ray sources continues to the present, e.g. Zhang [8], with more complete modelling of the source processes in accreting binary systems becoming a reality.

## Pulsar Timing Methods

There are two principal approaches to determining the period of a pulsar with accuracy: epoch folding, and Fourier transforms.

Epoch folding is essentially a brute force method of determining the pulse shape and period by refining an initial guess. The target intensity vs. time data is broken into segments matching the approximate period. The segments are stacked on top of each other and a histogram is produced for intensity over the period. If the approximate period is unrelated to the true period of the pulsar then there will be no correlation between the stacked data segments and the histogram will show a roughly flat, random distribution. On the other hand, if the period closely matches the true period then the segments will correlate and a pulse shape will be evident. Anything from a handful to hundreds of potential periods might be tried until a close match is found. Once a close match is found the fit can be optimised by tweaking the period in small increments until the difference between the distribution and a flat line is maximised. Typically, a  $\chi^2$  metric is used in the opposite sense to the way a statistician would use it, i.e. looking for a worst (maximal) value indicating a poor fit to a horizontal line.

The Fourier transform is a method of converting a continuous, periodic signal into a frequency domain representation. The transform makes use of

the knowledge that any periodic waveform can be represented by the summation of an infinite series of sinusoid waves or varying amplitude, phase, and frequency. The Fourier transform has an equivalent for use on discrete samples of a continuous function, called the discrete Fourier transform (DFT). Computational resource requirements have historically limited DFT use for astronomical purposes but several efficient means of computing the DFT, the most common of which is called the fast Fourier transform (FFT), coupled with vast increases in computing power have made Fourier analysis a more viable option. The correlation between time domain and frequency domain signals is depicted graphically in Figure 1. The time domain signal is sampled  $N$  times at  $\Delta T$  second intervals for a total time of  $T$  seconds. The FFT output is a complex representation of magnitude and phase at each of  $N$  frequency points  $\Delta f = 1/T$  Hertz apart. However, only the first half of the samples are useful, with the second half being a mirror image. The example FFT shows the original signal has components at 1 and 2 Hz, and the bump near 3 Hz is from a component at 3.1 Hz that has been spread out because it does not fall neatly on a frequency sample. When the FFT is used on pulsar intensity data peaks should be apparent at the pulse period of the pulsar. The relationship of  $\Delta f$  to sample time ( $T$ ) means that extreme timing accuracy requires long observation periods. This of particular importance in pulsar timing where changes in frequency over time are very small.

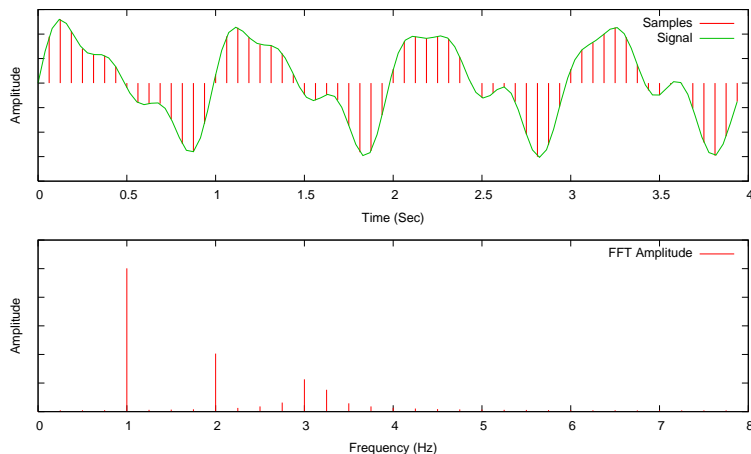


Figure 1: Time domain vs Frequency Domain. Top: Time varying signal sampled at  $N \times \Delta T$  intervals for a total of  $T$  secs. Bottom: Corresponding FFT output showing  $N/2$  samples at  $\Delta F = 1/T$  interval.

## Analysis

An analysis of RXTE data provided by Swinburne University was performed to determine the characteristics of two pulsar candidates. The data details, process, and results are outlined below.

### Data

The data provided by Professor Matthew Bailes of the Swinburne University of Technology has been collected from the RXTE PCA instrument. The data is for two X-ray pulsar objects:

- PSR B0540-69. PSR B0540-69 was discovered in the Large Magellanic Cloud by Seward, Harnden, and Helfund [5] in 1984.
- PSR B1509-58. PSR B1509-58 was discovered in 1982 by Seward and Harnden [4] using observations from the Einstein Observatory. The object was also observed in the radio frequency by Manchester, Tuohy, and Damico [3].

	Observation No.	Start (UTC)	Duration (sec)	No. of Events
B0540-69	1	11 Sep 1996 16:43:34	1930	235294
	2	12 May 1999 19:55:53	2157	160346
	3	13 Mar 2000 05:53:07	6932	459686
B1509-58	1	12 Jan 1997 03:08:05	3040	749457
	2	06 Jul 1997 08:30:37	2528	630625
	3	22 Dec 1997 00:19:43	2800	678991

Table 1: Summary of RXTE PCA Data

For each object, three observation periods are provided as summarised in Table 1. The data has been reduced and presented in the form of photon time-of-arrival in seconds referenced to the epoch 1 January 1984 00:00:00 UTC. The timing information is provided at the  $0.1\mu\text{s}$  level

### Processing

The processing method adopted for this data is using the FFT to extract dominant frequency components from the signals. The general processing steps used are:

- Bin Data. Take arrival time information spanning the desired sampling period and produce a histogram in  $\Delta T$  bins.

- Remove Bias. Remove any fixed bias, i.e. constant background, in the signal by subtracting the average counts per bin from each bin. This eliminates the potential of a substantial DC peak in the FFT output to obscuring low frequency variation.
- FFT. Perform the FFT and verify that the sampling rate was high enough to eliminate any aliasing effects. If aliasing is present, reduce the sampling time (bin size) and repeat the process.
- Identify Peaks. Identify candidate spectral peaks corresponding to the pulse frequency. The absolute magnitude of the spectral peaks is not of particular importance to this analysis.
- Recover Pulse. Verify the candidate pulse frequency by folding the data on the candidate period to recover the pulse shape. If the frequency is good then a pulse shape will emerge.

This processing was achieved using the GNU Octave mathematical package, which includes the FFTPACK implementation of the Cooley and Tukey FFT. Table 2 shows the parameters used for the Fourier transforms. Several considerations were made in choosing parameters for the FFT analysis of the available data:

- Frequency resolution. The spacing of samples in the frequency domain ( $\Delta f$ ) is driven by the total sampling time ( $T$ ) available in the time domain:  $\Delta f = 1/T$ . Bearing in mind the available sample sizes, the total observation time ( $T$ ) was set to 1000 (B0540-69) and 2000 (B1509-58) seconds giving a frequency increment of 1 and 0.5 milliHertz respectively.
- Cutoff frequency. The nature of the FFT gives  $N$  frequency domain samples out, for  $N$  time domain samples in. However, only the first  $N/2$  samples carry useful information: the first sample is a DC bias or average signal ( $f = 0$ ), and the remaining samples represent increments of  $\Delta f$  up to half the time domain sampling rate (the Nyquist criterion). From the literature the expected pulse frequency for B0540-69 and B1509-58 are  $\approx 20$  Hz and  $\approx 6$  Hz respectively. A sampling

	B0540-69	B1509-58	
$T$	1000	2000	seconds
$N$	131072	262144	samples
$\Delta t = T/N$	0.01526	0.00763	seconds
$\Delta f = 1/T$	0.001	0.0005	Hertz

Table 2: Parameters used in FFT runs for both target objects.

rate of 1000 Hz gives a frequency cutoff of 500 Hz which is more than adequate for the likely signals and any harmonics.

- FFT restrictions. The Octave FFT implementation requires a number of samples that is a power of two, i.e. 32, 64, etc. Selecting  $N = 2^{17}$  or  $N = 2^{18}$  as the number of samples allows a reasonably small sample time and good total time, thereby maintaining a high cutoff frequency and good frequency resolution.

## Results

The spectrum plots for the two pulsars are shown in Figure 2 and Figure 3. Both pulsars show clear peaks. B0540-69’s peaks are embedded in a noisy background and rise to approximately 6–9 times the average level. In contrast, the B1509-58 peaks are approximately 40 times the average, quiet background. Table 3 summarises the centre frequency derived by simple linear interpolation from the two strongest samples for both objects. In the case of PSR B1509-58 there are identifiable, lesser peaks at the second and third harmonics of the fundamental.

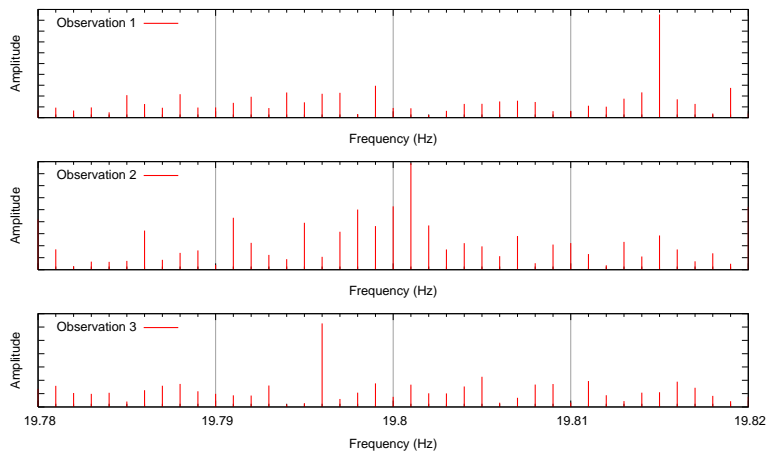


Figure 2: Frequency domain plots for PSR B0540-69. Shows the region around the largest peak in detail

## Discussion

The data clearly shows a decline in rotation frequency, i.e. an increase in pulse period ( $P$ ), for both objects. This is consistent with a braking force being applied to retard rotation. Current theory dictates that this braking force is produced predominantly by the interaction of a massive magnetic

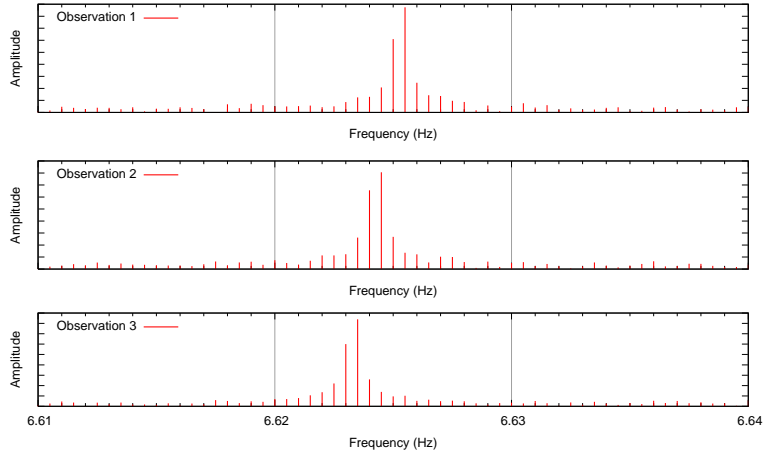


Figure 3: Frequency domain plot for PSR B1509-58. Shows the region around the largest peak in detail.

Object	Observation No.	Rot frequency ( $\Omega$ , Hz)	Period (millisec)
B0540-69	1	19.8148	50.467
	2	19.8006	50.503
	3	19.7961	50.515
B1509-58	1	6.62529	150.94
	2	6.62428	150.96
	3	6.62329	150.98

Table 3: Pulsar frequencies and period from FFT data.

field with the material surrounding the pulsar. A straight line fit of the pulsar period data allows determination of an assumed constant rate of period change. The rates, based on a least-squares linear fit, are shown in Table 4. The rate of period change,  $\dot{P} \equiv dP/dt$ , can be used to determine a *characteristic lifetime* for the pulsar by assuming that  $\dot{P}$  is constant and calculating the time required for the rotation to stop. Typically,  $\dot{P} \sim 10^{-15}$  and the characteristic lifetime is  $P/\dot{P} \sim 10^7$  years. However, for both pulsars studied here the  $\dot{P}$  is two orders of magnitude higher than typical, and the characteristic lifetimes (Table 4) are markedly shorter.

A similar figure for the *characteristic age* of the pulsar can also be derived, and is more often used. Derivation of this figure makes the assumption that the braking torque slowing rotational frequency ( $\Omega$ ) is proportional to some power of the rotational frequency, so  $\dot{\Omega} \propto \Omega^n$  where  $n$  is the braking index. If the original spin frequency of the pulsar is  $\Omega_0$  then the current age can be calculated:

$$t = -\frac{\Omega}{(n-1)\dot{\Omega}} \left[ 1 - \left( \frac{\Omega}{\Omega_0} \right)^{n-1} \right]$$

For braking by magnetic interaction alone theory gives  $n = 3$ . By assuming  $n = 3$  and that the current rotation is much slower than at first formation, i.e.  $\Omega \ll \Omega_0$ , the equation is simplified to:

$$\tau = -\frac{\Omega}{2\dot{\Omega}} = \frac{P}{2\dot{P}} \quad (1)$$

where  $\tau$  is the characteristic age. Characteristic ages for both pulsars are shown in Table 4. The actual braking index can be calculated by measurement of the second derivative of the rotational frequency and use of  $n = \Omega\ddot{\Omega}/\dot{\Omega}^2$ . The required measurements need high precision, long observations, and complicated processing and will not be attempted here.

The change in period directly relates to a loss of rotational kinetic energy due to braking. The expression for rotational kinetic energy is:

$$K = \frac{1}{2}I\omega^2 = \frac{2\pi^2 I}{P^2} \quad (2)$$

where  $\omega$  is the rotation rate in radians per second, and  $I$  is the moment of inertia. Equation (2) leads to the following expression for the rate of change of energy:

$$\frac{dK}{dt} = -\frac{4\pi^2 I \dot{P}}{P^3} \quad (3)$$

$$\approx -4.3 \times 10^{39} \frac{\dot{P}}{P^3} \quad (4)$$

Assuming a spherical neutron star of a typical size and mass,  $R = 10^4$  metres and  $M = 1.4M_\odot$ , gives  $I = 1.1 \times 10^{38} \text{kg m}^2$  reduces (3) to (4). The energy loss rates for B0540-69 and B1509-58 are shown in Table 4.

Continuing with the assumption that magnetic braking dominates the energy loss mechanisms ( $n = 3$ ) and a typical moment of inertia, we are able to determine an approximate magnetic field for the neutron star:

$$B \approx \left( \frac{3Ic^3 P \dot{P}}{8\pi^2 R^6} \right)^{1/2} \quad (5)$$

$$\approx 3.2 \times 10^{19} (P \dot{P})^{1/2} \quad (6)$$

Approximate magnetic field strengths for the two candidate pulsars are displayed in Table 4.

Object	PSR B0540-69	PSR B1509-58	
$\dot{P}$	$4.31 \times 10^{-13}$	$1.54 \times 10^{-12}$	$\text{s s}^{-1}$
Characteristic age	1854	1557	years
Characteristic life	3708	3114	years
Energy loss	$1.44 \times 10^{31}$	$1.92 \times 10^{30}$	Watts
Magnetic field	$4.7 \times 10^{12}$	$1.5 \times 10^{13}$	Gauss

Table 4: Pulsar  $\dot{P}$  and derived characteristics.

With the respective periods in hand, recovering the pulse shape from the sparse time-of-arrival data is now possible. By folding the TOA every period and then forming a histogram of the number of pulses we gain an insight into the pulse shape. 50 bins were used for each histogram. The recovered pulse profiles for each observation are shown in Figure 4. The pulse profile of B0540-69 is wide, very noisy, and poorly defined in comparison to the much cleaner profile of B1509-58. The difference in profile quality will be largely driven by the much lower signal to noise ratio of B0540-69 discussed earlier.

The derived rotational periods and first derivatives for the two targets compare favourably with figures drawn from the literature.

- PSR B0540-69. Seward *et al.* [5] give the B0540-69 pulsar period as  $P = 0.050208679(3)$  seconds. Cusumano, Massaron, and Mineo [1] give  $P = 0.050463$  on the day of the first observation, and 0.050503 and 0.050517 seconds on the day of the second and third observations respectively. Both Seward *et al.* and Cusumano *et al.* give  $4.79 \times 10^{-13}$  as the  $\dot{P}$  value. This study found a comparable value of  $4.31 \times 10^{-13} \text{s s}^{-1}$ .
- For PSR B1509-58 Seward and Harnden [4] gave  $P = 0.150084(1)$  seconds as the period and  $\dot{P} = 1.49 \times 10^{-12} \text{s s}^{-1}$ . The corresponding figures from Taylor, Manchester, and Lyne [7] are  $P = 0.1506575509200000\text{s}$  and  $\dot{P} = 1.5365291 \times 10^{-12} \text{s s}^{-1}$ .

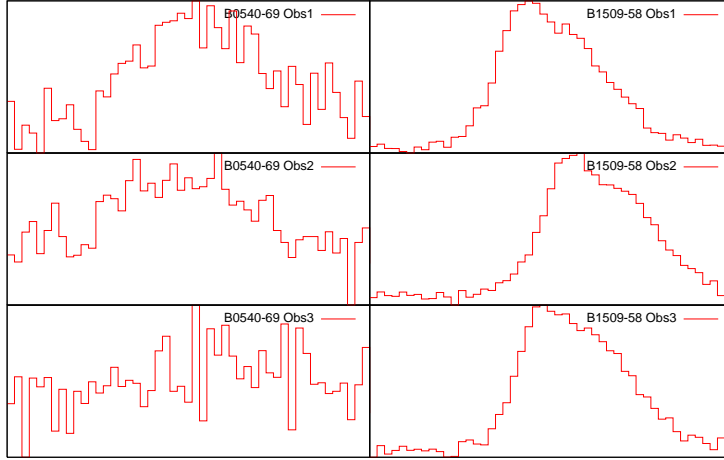


Figure 4: Pulse profiles for PSR B0540-69 (left) and PSR B1509-58 (right). Rough adjustment for phase has been made.

Figure 5 shows the target pulsar  $\dot{P}$  vs  $P$  overlaid on equivalent figures for 706 pulsars from Taylor *et al.* [7] and lines of equal lifetime and magnetic field. From the plot it is easily seen that the figures derived here are reasonably close the Taylor's figures for the same objects. PSR B0540-69 and PSR B1509-58 are clearly on the fringe of the main pulsar population which goes some way toward explaining the atypically low characteristic lifetime figures. The region surrounding the target pulsars is shared by a number of other pulsars associated with supernova remnants. Remnants have typical lifetimes of  $10^5$  years, which lends a degree of confidence to the characteristic age figures derived here.

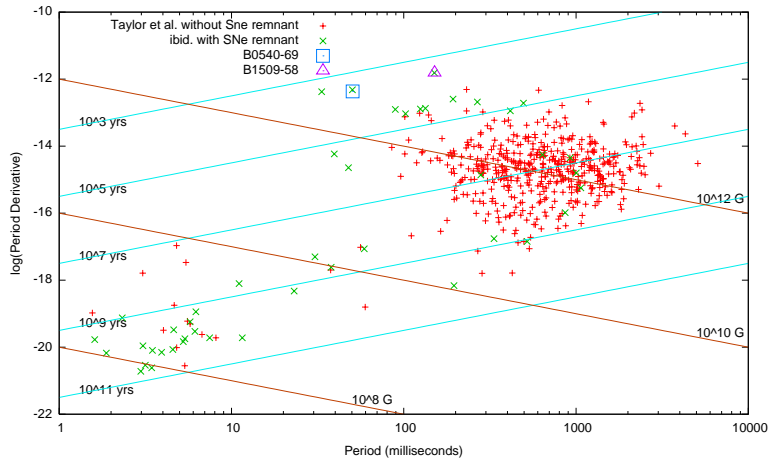


Figure 5: Pulsar Population. The target pulsars are indicated in context with 706 pulsars from the Taylor *et al.* tables.

## Conclusion

In this project the Rossi X-ray Timing Explorer and its science instruments were described. Areas of research in which RXTE features have been discussed. Data for two targets, taken from the RXTE Proportional Counter Array instrument, was analysed for the presence of pulsar signals. Signals were found in both data sets, for PSR B0540-69 with a rotation period of approximately 50 ms and PSR B1509-58 with a period of approximately 150 ms. Estimates of the rate of rotation slowing, characteristic age, rotational energy loss, and surface magnetic field were made. Despite the lower precision, the rotation rate, derivative, and derived values compare favourably with figures from different epochs by other researchers.

## References

- [1] G. Cusumano, E. Massaro, and T. Mineo. Timing noise, glitches and the braking index of PSR B0540-69. *A&A*, 402:647–652, May 2003.
- [2] K. Jahoda, C. B. Markwardt, Y. Radeva, A. H. Rots, M. J. Stark, T. E. Swank, J. H. Strohmayer, and W. Zhang. Calibration of the Rossi X-ray Timing Explorer Proportional Counter Array. In print, submitted to *ApJS* 19 Oct 2004. [http://hea-www.gsfc.nasa.gov/users/keith/pca/calibration\\_submitted.pdf](http://hea-www.gsfc.nasa.gov/users/keith/pca/calibration_submitted.pdf).
- [3] R. N. Manchester, I. R. Tuohy, and N. Damico. Discovery of radio pulsations from the X-ray pulsar in the supernova remnant G320.4-1.2. *ApJ*, 262:L31–L33, November 1982.
- [4] F. D. Seward and F. R. Harnden. A new, fast X-ray pulsar in the supernova remnant MSH 15-52. *ApJ*, 256:L45–L47, May 1982.
- [5] F. D. Seward, F. R. Harnden, and D. J. Helfand. Discovery of a 50 millisecond pulsar in the Large Magellanic Cloud. *ApJ*, 287:L19–L22, December 1984.
- [6] T. E. Strohmayer, W. Zhang, J. H. Swank, A. Smale, L. Titarchuk, C. Day, and U. Lee. Millisecond X-Ray Variability from an Accreting Neutron Star System. *ApJ*, 469:L9+, September 1996.
- [7] J. H. Taylor, R. N. Manchester, and A. G. Lyne. Catalog of Pulsars (Taylor+1995). *VizieR Online Data Catalog*, 7189:0+, November 2000.
- [8] C. Zhang. The MHD Alfvén wave oscillation model of kHz Quasi-Periodic Oscillations of Accreting X-ray binaries. *A&A*, 423:401–404, August 2004.
- [9] W. Zhang, I. Lapidus, N. E. White, and L. Titarchuk. KiloHertz Quasi-periodic Intensity Oscillations from 4U 1636-536. *ApJ*, 469:L17+, September 1996.